

Image Super-resolution Reconstruction Network based on Enhanced Swin Transformer via Alternating Aggregation of Local-Global Features

Yuming Huang¹, Yingpin Chen^{1*}, Changhui Wu¹, Hanrong Xie¹, Binhui Song¹, Hui Wang¹

(1. Minnan Normal University, School of Physics and Engineering, Zhangzhou, China, 363000)

Abstract: The Swin Transformer image super-resolution reconstruction network only relies on the long-range relationship of window attention and shifted window attention to explore features. This mechanism has two limitations. On the one hand, it only focuses on global features while ignoring local features. On the other hand, it is only concerned with spatial feature interactions while ignoring channel features and channel interactions, thus limiting its non-linear mapping ability. To address the above limitations, this paper proposes enhanced Swin Transformer modules via alternating aggregation of local-global features. In the local feature aggregation stage, we introduce a shift convolution to realize the interaction between local spatial information and channel information. Then, a block sparse global perception module is introduced in the global feature aggregation stage. In this module, we reorganize the spatial information first, then send the recombination information into a dense layer to implement the global perception. After that, a multi-scale self-attention module and a low-parameter residual channel attention module are introduced to realize information aggregation at different scales. Finally, the proposed network is validated on five publicly available datasets. The experimental results show that the proposed network outperforms the other state-of-the-art super-resolution networks.

Keywords: Image Super-resolution; Swin Transformer; Spatial and Channel Information Interaction; Block Sparse Global-awareness; Multi-Scale Self Attention

* **Corresponding author:** Yingpin Chen is the corresponding author of this work. He is now an associate professor in Minnan Normal University. His E-mail is 110500617@163.com.

Funding information: This work is supported by national natural science foundation of China (62001199), the natural science foundation project of Fujian Province (2023J01155), the natural science foundation project of Zhangzhou City (ZZ2023J37), the principal foundation of Minnan Normal University (KJ19019), the high-level science research project of Minnan Normal University (GJ19019), research project on education and teaching of undergraduate colleges and universities in Fujian Province (FBJY20230083), and the education research program of Minnan Normal University (202211).

Conflict of Interest statement: This manuscript has not been published or presented elsewhere in part or in entirety and is not under consideration by another journal. We have read and understood your journal's policies, and we believe that neither the manuscript nor the study violates any of these. There are no conflicts of interest to declare.

Permission to reproduce materials from other sources: None.

Data Availability statement: All data, models, or code generated or used during the study are available from the corresponding author by request.

1 Introduction

Image super-resolution (SR) reconstruction is a classical problem in image processing, which mainly generates images with high spatial resolution and clear details [1-4]. The essence of image SR is to recover the high-frequency components lost in low-resolution images. Image SR reconstruction has been widely used in the fields of remote sensing imaging[1], infrared imaging[2, 3], medical imaging[4], and other fields.

There are three approaches for SR reconstruction, including interpolation-based method, model-driven-based method, and data-driven-based method. The algorithm based on interpolation[5] has been widely employed due to its simplicity and efficiency. However, the reconstruction results based on this algorithm have problems such as jaggedness and blurring, which seriously affect the quality of SR images. The model-driven-based [6, 7] method utilizes the prior knowledge of the image to recover detailed information. This kind of method has limitations in engineering applications due to their large computational complexity. With the development and maturity of parallel computing technology, the data-driven-based method has received widespread attention from scholars. For example, Dong *et al.* [8] proposed an SRCNN model via only three convolutional layers for image SR reconstruction. The SRCNN model adopts convolutional neural networks (CNN) for image SR reconstruction and achieves better reconstruction results than the ones via interpolation-based and model-driven-based methods. Subsequently, researchers improved the feature representation of the network model by increasing the network depth. For instance, Simonyan *et al.* [9] proposed a VGG network with a depth of 19 layers. Similarly, He *et al.* [10] proposed a ResNet model with 152 layers, adopting residual learning to avoid network gradient vanishing or exploding. Furthermore, Ledig *et al.* [11] combined a residual generation network with a discriminator network to propose an SRGAN model.

All of the above data-driven based methods adopt a convolutional structure. Although these convolution-based data-driven methods offer significant improvements in image reconstruction performance compared to traditional model-driven-based methods, they still face two fundamental problems. First, the interaction between the image and the convolution kernel is content-independent. Thus, using the same convolutional kernel to recover different image regions may not be a proper choice. Second, the convolution is limited for long-range dependency modeling [12]. As a result, the number of network layers must be increased to expand the receptive field, causing a large overhead of computational resources. Fang *et al.* [13] proposed combining CNN with Transformer to solve this problem. The method aggregates local and global features of an image but ignores the interaction of spatial and channel features, so there is still room for

improvement. Inspired by [13], an image SR reconstruction network based on an enhanced Swin Transformer via alternating aggregation of local-global features is proposed in this paper as a way to improve the receptive field of the Swin Transformer network [14]. In the local feature aggregation stage, a shifted convolution structure is proposed to realize the extraction of local spatial features and the interaction of spatial-channel features. In the global feature aggregation stage, a global sparse is employed for the perception module based on multi-layer perceptron (MLP) and a multi-scale attention perception module to expand the receptive field. The detailed structure of the proposed network is shown later.

The Transformer [16-18] model has the ability to perceive information globally and thus has received extensive attention from researchers in computer vision. Recently, related studies in target detection [19], target classification [20], and video classification [21] have shown the great potential of the Transformer [22-26] model in the field of computer vision. For example, a vision transformer (ViT) [20] has adopted a Transformer to learn long-range dependencies on non-overlapping image blocks and obtained superior classification performance. However, ordinary attention with the quadratic complexity of input length is difficult to adapt in visual tasks where high-resolution images are the input. Liu et al. [27] proposed a Swin Transformer model to compute self-attention in a window, which reduces computational complexity and improves the local feature extraction ability of the model. However, the fixed window size constrains the Swin Transformer model's ability to handle objects at different scales. For this reason, a multi-scale window is introduced in the Swin Transformer block to improve the multi-scale learning ability of the model.

In recent years, the MLP model with channel and spatial information interaction has received much attention for its effective information interaction and simple network structure. For example, Tolstikhin et al. proposed the MLP-Mixer model [15], which increases the receptive field of the model by performing inter-channel and inter-space MLP operations on feature tensors. Moreover, Liu et al. [28] introduced a spatial gating unit (SGU) in MLP and proposed a gated multi-layer perceptron (gMLP) model. This model allows information to be interacted in different channels and spatial locations, thus improving the non-linear mapping ability of the model. Benefiting from the global receptive field of gMLP, Tu et al. proposed a MAXIM [29] model with linear complexity. Inspired by MAXIM, a block sparse global-awareness module (BSGM) is proposed to realize a large receptive field via global information reshaping and MLP.

This paper proposes the enhanced Swin Transformer super-resolution reconstruction network (ESTN) with alternating local-global feature aggregation to improve the Swin Transformer's long-range information interaction capability. In addition, to select channels for features without introducing plenty of parameters, a low-parametric residual channel attention block (LRCAB) is

designed. Finally, a local attribution map (LAM) [30] is adopted to analyze the size of ESTN's receptive field.

In summary, the main contributions of the proposed ESTN are as follows:

(1) This paper proposes an enhanced Swin Transformer module via alternating aggregation of local-global features. On the one hand, this module accomplishes the aggregation between local and global features through alternating structures. On the other hand, this module extracts the global feature, thus realizing a large receptive field to improve the non-linear mapping capability of the network.

(2) A multi-scale window attention mechanism is introduced to construct more flexible spatial long-range feature interactions. On the one hand, the small-size window helps to reduce the amount of window attention computation. On the other hand, the large-scale window helps to improve the model receptive field. Therefore, the multi-scale window attention mechanism achieves a balance between the receptive field and computational complexity. Compared to the fixed-window-size window attention mechanism, the proposed network avoids the high-complexity operation quadratic to the processing token length of the global window attention mechanism. Furthermore, it mitigates the problem of limited long-range modeling capability caused by the fixed-window-size.

(3) The feed-forward network (FFN) amplifies the number of feature channels through a linear layer, resulting in redundancy between channels and thus hindering feature expressiveness. To solve this problem, this paper designs a low-parameter residual channel attention module into the traditional FFN. In this way, it assigns channel attention to each channel without increasing too many network parameters and effectively solves the channel redundancy problem of FFN.

(4) Local attribution maps are brought into the experiments as a tool to visualize and analyze the receptive field of the proposed model. Experiments show that the receptive field of the proposed model exceeds that of other comparative Transformer-based super-resolution reconstruction networks. Thus, we reveal the reason for the prominent image reconstruction performance of the proposed model and further verify the validity of the local-global alternating feature aggregation idea.

2 Preparatory knowledge

2.1 Image super-resolution

Images are often degraded by various factors during transmission, resulting in loss of information and thus affecting the quality of the image. Low-resolution (LR) images degraded from high-resolution (HR) images may suffer from edge blurring, an artifact caused by

downsampling. The image SR reconstruction technique recovers the image detail with high resolution from the LR image.

Researchers have conducted much research in image SR reconstruction to overcome the image degradation problem. In recent years, deep learning-based image SR reconstruction techniques have rapidly developed. These techniques learn the mapping of low-resolution images to high-resolution images from large-scale paired datasets. To improve the performance of SR reconstruction models, some models incorporate more refined neural network architectures, such as residual connection [11], dense connectivity [31], *etc.* Some other SR reconstruction networks apply attention mechanisms [16, 32] in the CNN framework and achieve excellent reconstruction performance.

2.2 Swin Transformer model

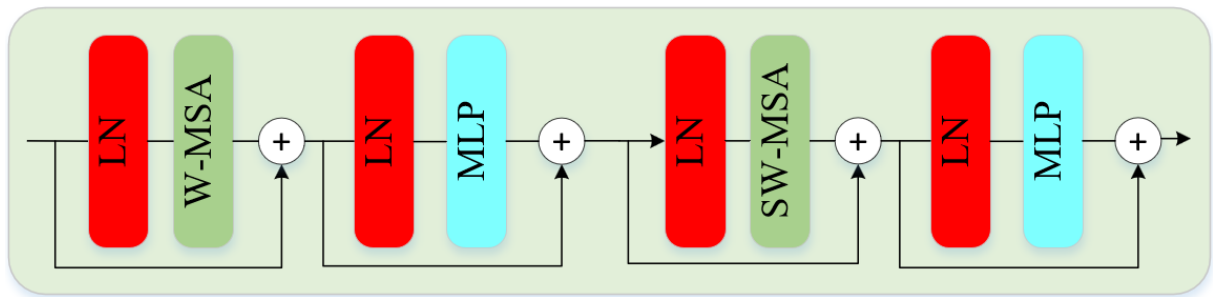


Fig. 1 Swin Transformer module.

Recently, the Transformer [16] model in natural language processing has been widely used in computer vision [19, 20]. The Transformer has a larger receptive field than CNN-based networks, so it performs better in image processing than CNN-based networks [15] and has been employed in image SR reconstruction [12, 33]. For example, ViT [20] has demonstrated great potential as an alternative to CNN models. Although ViT achieves favorable performance, its computational complexity is squarely related to the length of the processed token. In order to enhance the computational efficiency of ViT, the Swin Transformer [27] introduced the concept of shifted window self-attention. This innovation reduces computational effort while enabling neighboring windows to interact with information. As shown in Fig. 1, the Swin Transformer block successively computes window multi-head self-attention (W-MSA) shifted window multi-head self-attention (SW-MSA) modeling the local region texture information of the image. The MLPs in Fig. 1 have two forward feed layers with a GELU[34] activation between the layers for further feature transformations. Before each MSA module and MLP module, a layer normalization (LN) [35] is applied. A residual connection is applied after each module. Due to the small window attention computation of the Swin Transformer model, the model has the advantage of dealing with large-scale images. The SwinIR[12] model applies the Swin Transformer to SR reconstruction

and achieves outstanding performance metrics as well as computational efficiency.

Since MSA computes self-attention directly on the sequence, MSA increases the model's computational complexity and training time. The W-MSA proposed by Swin Transformer limits the scope of attentional computation to a window, making it more advantageous and less computationally complex when dealing with large-scale data or long sequences. However, the W-MSA of the Swin Transformer focuses only on spatial feature interactions and ignores the channel feature interactions, limiting the non-linear mapping capability. Therefore, this paper introduces shift convolution units based on the Swin Transformer to improve the model's spatial and channel information interaction capability.

3 Proposed network

To make the model globally perceptive and avoid adding too many parameters. This paper proposes an Enhanced Swin Transformer Network (ESTN) via alternating aggregation of local-global features for image super-resolution. In addition, to analyze the effect of the proposed ESTN network on the receptive field, we introduce the LAM to visualize the receptive field of the reconstructed network.

3.1 Network architecture

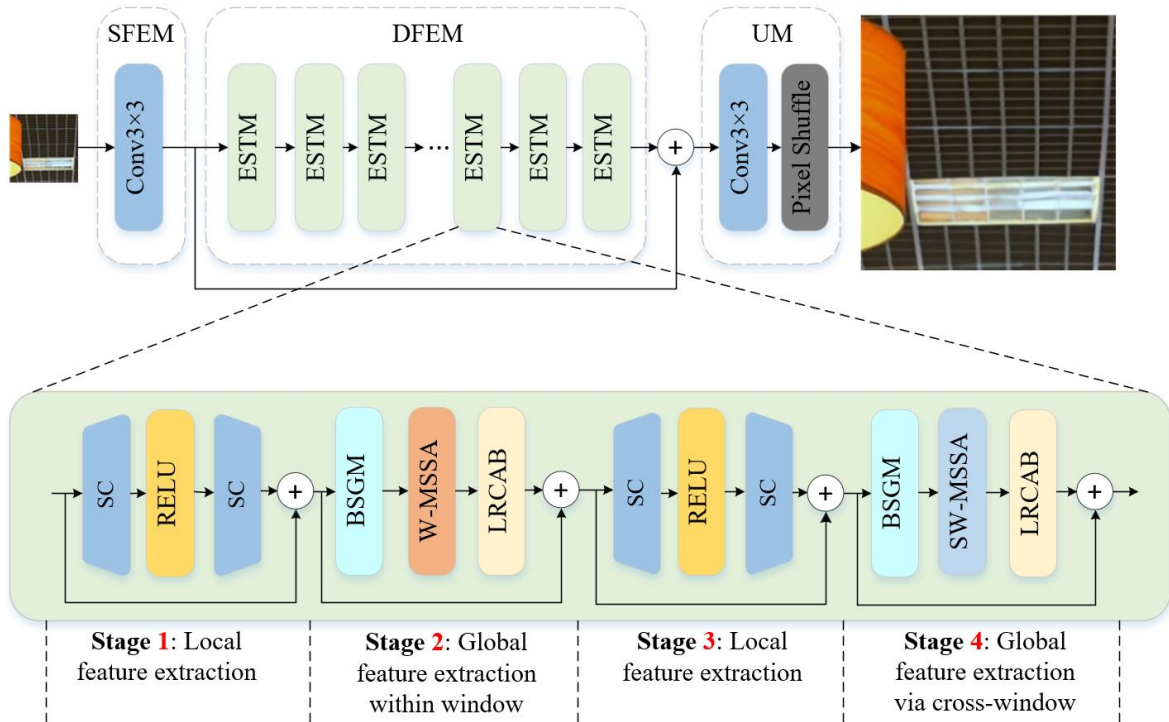


Fig. 2 Enhanced Swin Transformer image super-resolution reconstruction network

As shown in Fig. 2, the proposed SR reconstruction network ESTN consists of three components: the shallow feature extraction module (SFEM), the deep feature extraction

module (DFEM), and the up-sampling module (UM). SFEM uses a 3×3 convolution to extract shallow features. The DFEM consists of several enhanced Swin Transformer modules (ESTM). First, local features are extracted using two shift-convolution (SC) [36], which facilitates the model to recover a fine texture. Subsequently, we employ the block sparse global-awareness module (BSGM), window multi-scale self-attention (W-MSSA), and low-parametric residual channel attention block (LRCAB) as modules for the second stage of global feature extraction. Finally, feature extraction is alternately performed for both local and global features. The distinction lies in the fourth stage, where the window multi-scale self-attention incorporates a shift operation. The shifted window multi-scale self-attention (SW-MSSA) facilitates inter-window information interaction. UM consists of a 3×3 convolution and pixel shuffle [37], which enables the output of SR images by enlarging the image by a specified magnification.

3.1.1 Shallow and deep feature extraction

Given an LR image $\mathcal{I}_L \in \mathbb{R}^{3 \times H \times W}$, shallow features are extracted using a convolution with a spatial resolution of 3×3 , where each slice convolution operation is defined as:

$$\mathcal{F}_0(c, :, :) = \mathcal{W}_0^{3 \times 3}(c, :, :, :) * \mathcal{I}_L, \quad (1)$$

where $\mathcal{W}_0^{3 \times 3}(c, :, :, :)$ denotes the c -th ($c = 1, 2, \dots, C$) convolutional kernel in convolutional kernel set $\mathcal{W}_0^{3 \times 3} \in \mathbb{R}^{C \times 3 \times 3 \times 3}$ with a spatial resolution of 3×3 ; $\mathcal{F}_0 \in \mathbb{R}^{C \times H \times W}$ is a shallow feature; $\mathcal{F}_0(c, :, :)$ denotes the c -th level slice of the convolution result; c denotes the number of channels for intermediate features; $*$ denotes the convolution operator. For simplicity of expression, subsequent convolutions only express the relationship between the convolution kernel, the convolved tensor, and the convolution result analogously to $\mathcal{F}_0 = \mathcal{W}_0^{3 \times 3} * \mathcal{I}_L$.

$$\mathcal{F}_D = F_D(\mathcal{F}_0), \quad (2)$$

where F_D denotes DFEM; $\mathcal{F}_D \in \mathbb{R}^{C \times H \times W}$ denotes deep features extracted by DFEM.

$$\begin{cases} \mathcal{F}_i = F_{E_i}(\mathcal{F}_{i-1}), i = 1, 2, \dots, I-1, \\ \mathcal{F}_D = F_{E_I}(\mathcal{F}_{i-1}), i = I, \end{cases} \quad (3)$$

where $F_{E_i}, i = 1, \dots, I$ denotes the i -th ESTM; $\mathcal{F}_i, i = 1, \dots, I-1$ denotes the i -th ESTM output feature.

3.1.2 Up-sampling module

The SR image can be recovered by summing the shallow feature \mathcal{F}_0 and deep feature \mathcal{F}_D , followed by 3×3 convolution and pixel shuffle.

$$\mathcal{I}_S = F_P(\mathcal{W}_1^{3 \times 3} * (\mathcal{F}_D + \mathcal{F}_0)), \quad (4)$$

where F_P denotes a pixel shuffle[37] operation; $\mathcal{I}_S \in \mathbb{R}^{3 \times aH \times aW}$ denotes the SR image where a is a magnification ratio; $\mathcal{W}_1^{3 \times 3} \in \mathbb{R}^{C \times C \times 3 \times 3}$ denotes a convolutional kernel with a spatial resolution of 3×3 .

3.1.3 Loss function

We use Adam [38] as the optimizer to optimize the parameters of the ESTN by minimizing the L_1 loss:

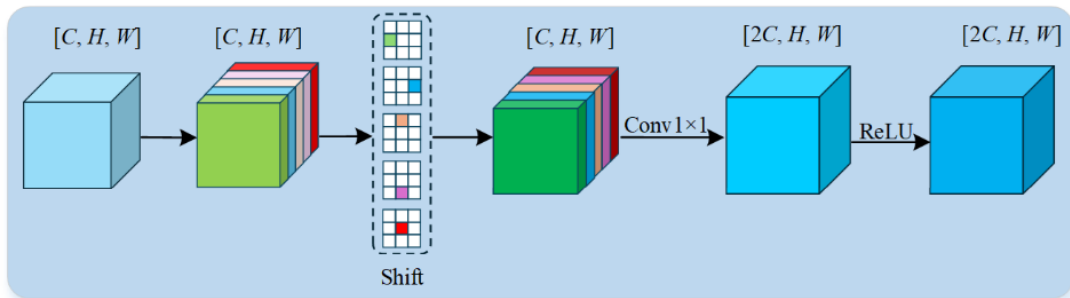
$$L = \frac{1}{N} \sum_{n=1}^N \|\mathcal{I}_{S,n} - \mathcal{I}_{H,n}\|_1, \quad (5)$$

where $\mathcal{I}_{S,n}$ and $\mathcal{I}_{H,n}$ denote the n -th ($n = 1, 2, \dots, N$) (N denotes the number of batches) SR and HR images in the batch, respectively.

3.2 Enhanced Swin Transformer model

Existing Swin Transformer-based image super-resolution (SR) reconstruction networks are limited by the small size of the attention window, leading to a constrained ability to construct long-range dependencies. This limitation leads to the poor quality of the recovered high-resolution images. To solve this problem, this paper introduces BSGM in Swin Transformer so that the reconstructed network can construct the long-range dependency better. At the same time, the MSA of Swin Transformer is replaced with MSSA focusing on multi-scale information. The following introduces the signal flow diagram of each stage in ESTM one by one.

3.2.1 Stage 1: Local feature extraction stage



(a)

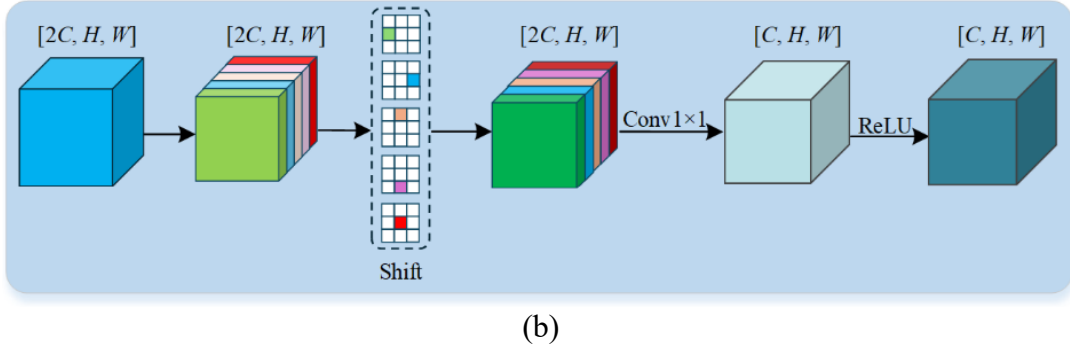


Fig. 3 Shift convolution schematic. (a) Channel expansion shift convolution; (b) Channel compressed shift convolution.

Fig. 3 shows details of the first stage of localized feature aggregation in Fig. 2. As shown in Fig. 4(a), the features undergo SC and 1×1 convolution to extract local features and expand the channel dimension, respectively.

$$\mathcal{F}_{i,e_0} = \sigma\left(\mathcal{W}_{i,e_0}^{1 \times 1} * D_C\left(\mathcal{W}_{i,s_0}, \mathcal{F}_{i-1}\right)\right), \quad (6)$$

where $\mathcal{W}_{i,s_0} \in \mathbb{R}^{C \times 3 \times 3}$ denotes the SC kernel that stacks five groups of convolution kernels along the channel, as shown in Fig. 4(a); D_C denotes the channel direction layer-by-layer convolution operator; $\mathcal{W}_{i,e_0}^{1 \times 1} \in \mathbb{R}^{2C \times C \times 1 \times 1}$ denotes the 1×1 convolution kernel for channel dimension expansion; σ denotes the RELU [39] activation function; $\mathcal{F}_{i,e_0} \in \mathbb{R}^{2C \times H \times W}$ denotes the feature after channel dimension expansion.

As shown in Fig. 3(b), the feature \mathcal{F}_{i,e_0} undergoes SC, followed by channel dimension compression using a 1×1 convolution kernel to align with the channel dimension of the input feature \mathcal{F}_{i-1} .

$$\mathcal{F}_{i,c_0} = \sigma\left(\mathcal{W}_{i,c_0}^{1 \times 1} * D_C\left(\mathcal{W}_{i,s_1}, \mathcal{F}_{i,e_0}\right)\right), \quad (7)$$

where $\mathcal{W}_{i,s_1} \in \mathbb{R}^{2C \times 3 \times 3}$ denotes the SC kernel that moves the features in space; $\mathcal{W}_{i,c_0}^{1 \times 1} \in \mathbb{R}^{C \times 2C \times 1 \times 1}$ denotes the 1×1 convolution kernel for channel dimension compression; $\mathcal{F}_{i,c_0} \in \mathbb{R}^{C \times H \times W}$ denotes the feature after for channel dimension compression.

Local feature \mathcal{F}_{i,o_1} is obtained through residual connections of feature \mathcal{F}_{i-1} with feature \mathcal{F}_{i,c_0} after channel dimension compression.

$$\mathcal{F}_{i,o_1} = \mathcal{F}_{i,c_0} + \mathcal{F}_{i-1}. \quad (8)$$

3.2.2 Stage 2: Global feature extraction stage

3.2.2.1 Block sparse global-awareness module in stage 2

This paper adopts the BSGM to construct sparse global awareness of features.

$$\mathcal{F}_{i,B_0} = F_{i,B_0}(\mathcal{F}_{i,o_1}), \quad (9)$$

where F_{i,B_0} denotes the BSGM of stage 2 in the i -th ESTM.

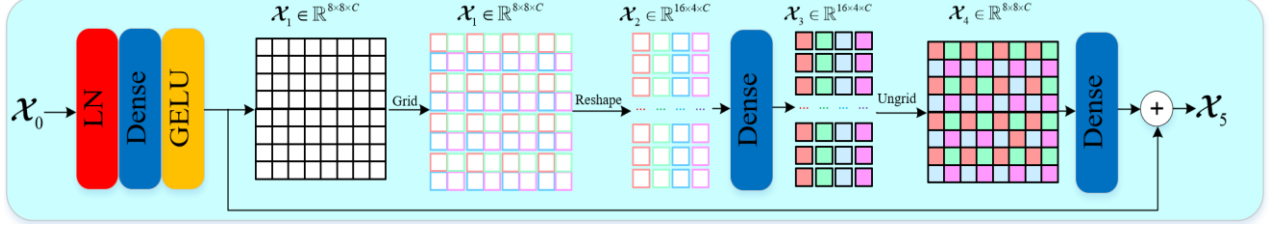


Fig. 4 Schematic of the block sparse global-awareness module.

As shown in Fig. 4, the input tensor is assumed to be $\mathcal{X}_0 \in \mathbb{R}^{8 \times 8 \times C}$. \mathcal{X}_0 is normalized by layer normalization, channel dimension feature mapping, and GELU[34] activation function to obtain $\mathcal{X}_1 \in \mathbb{R}^{8 \times 8 \times C}$:

$$\mathcal{X}_1 = g(D(LN(\mathcal{X}_0))), \quad (10)$$

where D denotes the dense layer shown in Fig. 4. It is implemented by a fully connected feature mapping.

Feature \mathcal{X}_1 performs a spatial mapping to obtain \mathcal{X}_2 :

$$\mathcal{X}_2 = Reshape(Grid(\mathcal{X}_1)), \quad (11)$$

where $Grid$ denotes partitioning of the tensor by region (To facilitate drawing, Fig. 5 employs 2×2 as the window size of $Grid$ to express the information reorganization process. In the proposed network architecture, we set the window size of the $Grid$ to 4×4 .); $Reshape$ denotes changing the spatial arrangement of the tensor.

$$\mathcal{X}_3 = D(\mathcal{X}_2). \quad (12)$$

$$\mathcal{X}_4 = Ungrid(\mathcal{X}_3), \quad (13)$$

where $Ungrid$ denotes that the recovery tensor is the original shape.

A fully connected feature mapping is performed in the channel direction on the tensor \mathcal{X}_4 . After full connection the tensor \mathcal{X}_4 is residually connected to the tensor \mathcal{X}_1 to obtain the tensor \mathcal{X}_5 .

$$\mathcal{X}_5 = D(\mathcal{X}_4) + \mathcal{X}_1. \quad (14)$$

3.2.2.2 Window multi-scale self-attention module in stage 2

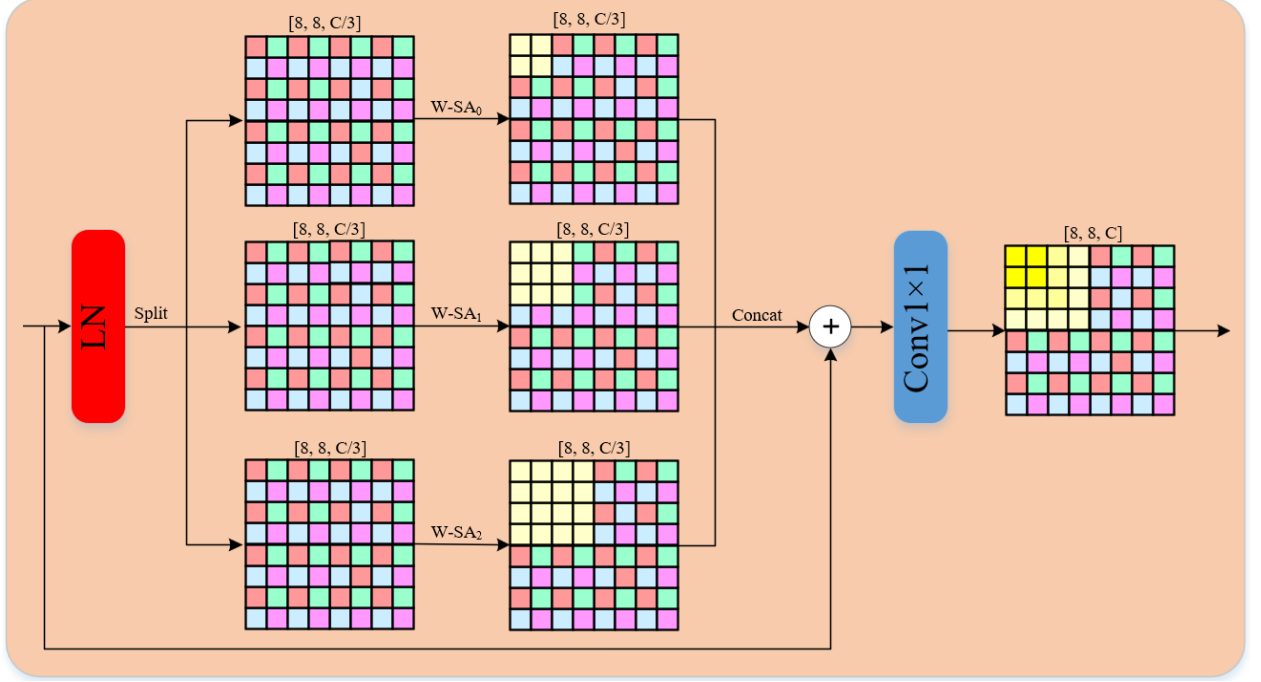


Fig. 5 Schematic of the window multi-scale self-attention.

In this paper, the introduction of MSSA enables the model to learn multi-scale information.

$$\mathcal{F}_{i,W} = F_{i,W}(\mathcal{F}_{i,B_0}), \quad (15)$$

where $F_{i,W}$ denotes the W-MSSA module for stage 2 of the i -th ESTM.

The MSSA is employed to compute multi-scale self-attention after the BSGM establishes sparse global awareness of the features. As shown in Fig. 5, the tensor is first divided into three equal parts from the channel dimension. Subsequently, attention matrices are computed using the windowed self-attention (W-SA_s ($s=0,1,2$)) module for each of the three scales to handle objects at various scales. The self-attention ranges are indicated in yellow. Self-attention matrix acquisition is shown in Fig. 6, where the query matrix \mathbf{Q} , key matrix \mathbf{K}^T , and value matrix \mathbf{V} are acquired via 1×1 convolution, respectively. This paper uses reflective padding at the boundaries of the image to ensure that the image size is an integer multiple of the size of each window.

$$\text{Attention}(\mathbf{Q}, \mathbf{K}, \mathbf{V}) = \text{SoftMax}\left(\frac{\mathbf{Q}\mathbf{K}^T}{\sqrt{h_s w_s}}\right)\mathbf{V}, \quad (16)$$

where $\text{SoftMax}(\mathbf{X})$ is an operator that takes the exponential of every element of a matrix \mathbf{X} and then normalizes each row independently to sum to one; $[h_s, w_s]$ ($s = 0,1,2$) indicates the size of the

local window.

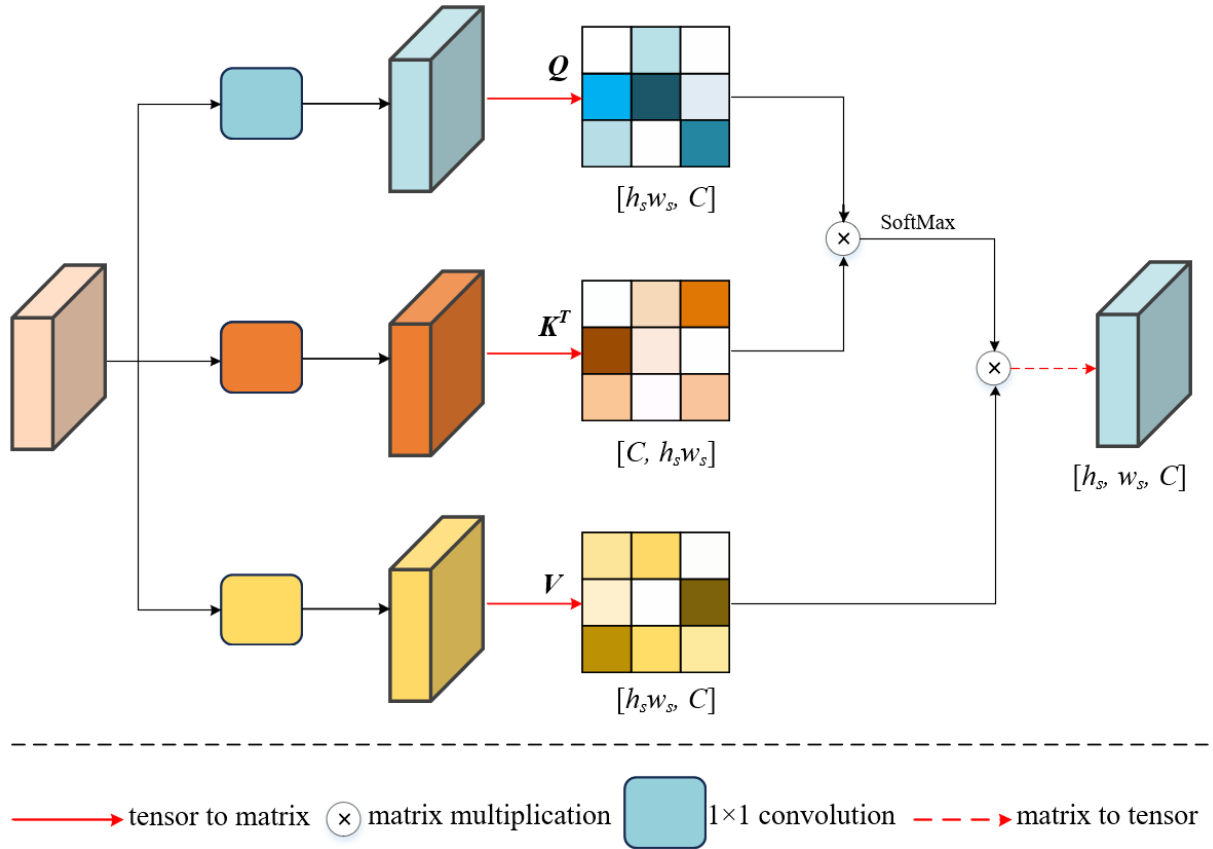


Fig. 6 Self-attention mapping illustration.

3.2.2.3 Low-parametric residual channel attention module in stage 2

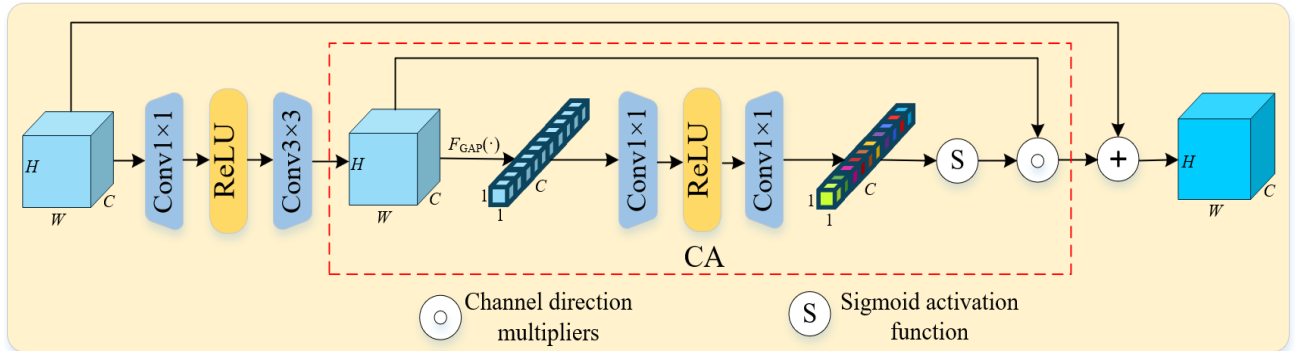


Fig. 7 Schematic of the low-parametric residual channel attention module.

The attention mechanism has recently been widely applied in image processing because of its outstanding performance. Due to the varying contributions of each channel feature to the super-resolution reconstruction results, this paper aims to introduce channel attention to focus on the channels of the features selectively.

As shown in Fig. 7, the dimensionality of the input feature $\mathcal{F}_i \in \mathbb{R}^{C \times H \times W}$ is expanded via 1×1 convolution. Expanding the dimensionality of the features can yield richer features, such as texture features with different directions and frequencies. Then, these features are used to learn and

recover the features to the same dimension as the input features using a 3×3 convolution. Lastly, the feature channels are selected via the channel attention module.

$$\mathcal{F}_{i,C} = F_C \left(\mathcal{W}_{i,c_1}^{3 \times 3} * \sigma \left(\mathcal{W}_{i,e_1}^{1 \times 1} * \mathcal{F}_{i,W} \right) \right) + \mathcal{F}_{i,W}, \quad (17)$$

where $\mathcal{W}_{i,e_1}^{1 \times 1} \in \mathbb{R}^{2C \times C \times 1 \times 1}$ denotes the 1×1 convolution kernel for channel dimension expansion;

$\mathcal{W}_{i,c_1}^{3 \times 3} \in \mathbb{R}^{C \times 2C \times 3 \times 3}$ denotes the 3×3 convolution kernel for channel dimension compression;

$$F_C(\mathcal{X}) = \text{Sigmoid} \left(\mathcal{W}_{i,e_2}^{1 \times 1} * \sigma \left(\mathcal{W}_{i,c_2}^{1 \times 1} * F_{\text{GAP}}(\mathcal{X}) \right) \right) \circ \mathcal{X}, \quad (18)$$

where $\mathcal{W}_{i,e_2}^{1 \times 1} \in \mathbb{R}^{2C \times C \times 1 \times 1}$ denotes the 1×1 convolution kernel for channel dimension expansion;

$\mathcal{W}_{i,c_2}^{1 \times 1} \in \mathbb{R}^{C \times 2C \times 1 \times 1}$ denotes the 3×3 convolution kernel for channel dimension compression; F_{GAP}

denotes the 2D global average pooling function; *Sigmoid* is the activation function; \circ denotes the channel direction multiplication symbol.

The tensor \mathcal{F}_{i,o_1} is residually connected to the tensor $\mathcal{F}_{i,C}$ to obtain the tensor \mathcal{F}_{i,o_2} .

$$\mathcal{F}_{i,o_2} = \mathcal{F}_{i,o_1} + \mathcal{F}_{i,C}. \quad (19)$$

3.2.3 Stage 3: Local feature extraction stage

Eqs. (20)-(21) illustrate the mathematical expressions for the third stage of localized feature extraction in Fig. 3, similar to stage 1.

$$\mathcal{F}_{i,e_3} = \sigma \left(\mathcal{W}_{i,e_3}^{1 \times 1} * D_C \left(\mathcal{W}_{i,s_0}, \mathcal{F}_{i,C} \right) \right), \quad (20)$$

$$\mathcal{F}_{i,o_3} = \mathcal{W}_{i,c_3}^{1 \times 1} * D_C \left(\mathcal{W}_{i,s_1}, \mathcal{F}_{i,e_3} \right) + \mathcal{F}_{i,o_2}, \quad (21)$$

where $\mathcal{W}_{i,e_3}^{1 \times 1} \in \mathbb{R}^{2C \times C \times 1 \times 1}$ denotes the 1×1 convolution kernel for channel dimension expansion;

$\mathcal{W}_{i,c_3}^{1 \times 1} \in \mathbb{R}^{C \times 2C \times 3 \times 3}$ denotes the 3×3 convolution kernel for channel dimension compression; \mathcal{F}_{i,s_1}

denotes the localized features of the shifted convolutional output of the third stage in ESTM.

3.2.4 Stage 4: Global feature extraction stage

3.2.4.1 Block sparse global-awareness module in stage 4

Eq. (22) illustrates the mathematical expression for learning sparse global awareness at stage 4 of the ESTM in Fig. 2, similar to BSGM in stage 2.

$$\mathcal{F}_{i,B_1} = F_{i,B_1} \left(\mathcal{F}_{i,o_3} \right), \quad (22)$$

where F_{i,B_1} denotes the BSGM of stage 4 in the i -th ESTM.

3.2.4.2 Shifted window multi-scale self-attention module in stage 4

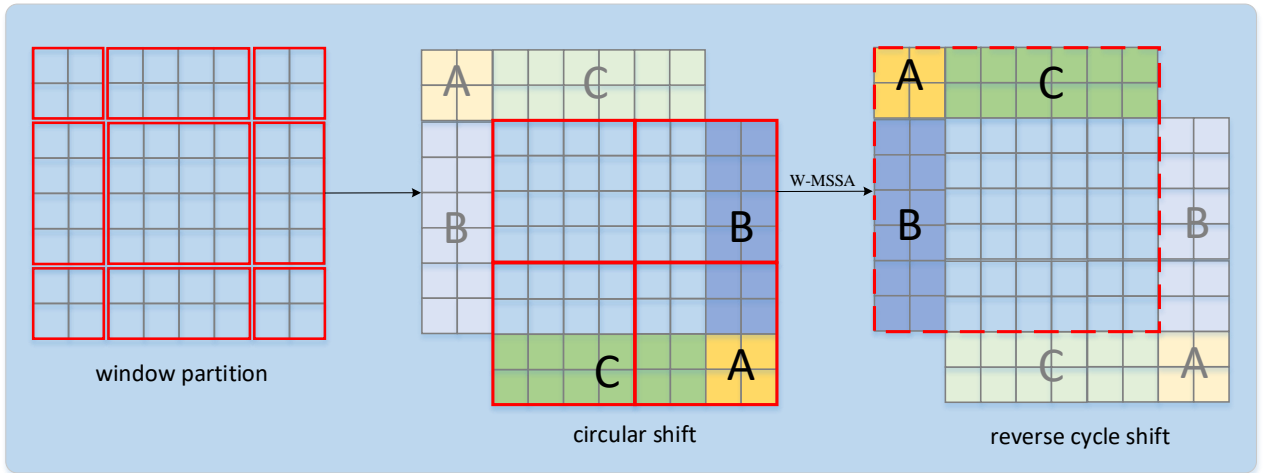


Fig. 8 Shift window multi-scale self-attention.

As shown in Fig. 8, SW-MSSA adds cyclic shift and inverse cyclic shift operations compared to W-MSSA. The cyclic shift distance is half of the current window size. The shift window multi-scale attention is computed by Eq. (23).

$$\mathcal{F}_{i,SW} = F_{i,SW}(\mathcal{F}_{i,B_1}), \quad (23)$$

where $F_{i,SW}$ denotes the SW-MSSA module in stage 4 of the i -th ESTM.

3.2.4.3 Low-parameter residual channel attention module in stage 4

Like LRCAB in stage 2, channel attention is computed to reassign channel weights.

$$\begin{cases} \mathcal{F}_i = F_{i,L_1}(\mathcal{F}_{i,SW}) + \mathcal{F}_{i,o_3}, i = 1, 2, \dots, I-1, \\ \mathcal{F}_D = F_{i,L_1}(\mathcal{F}_{i,SW}) + \mathcal{F}_{i,o_3}, i = I, \end{cases} \quad (24)$$

where F_{i,L_1} denotes the LRCAB in stage 4 of the i -th ESTM.

3.3 Local attribution maps

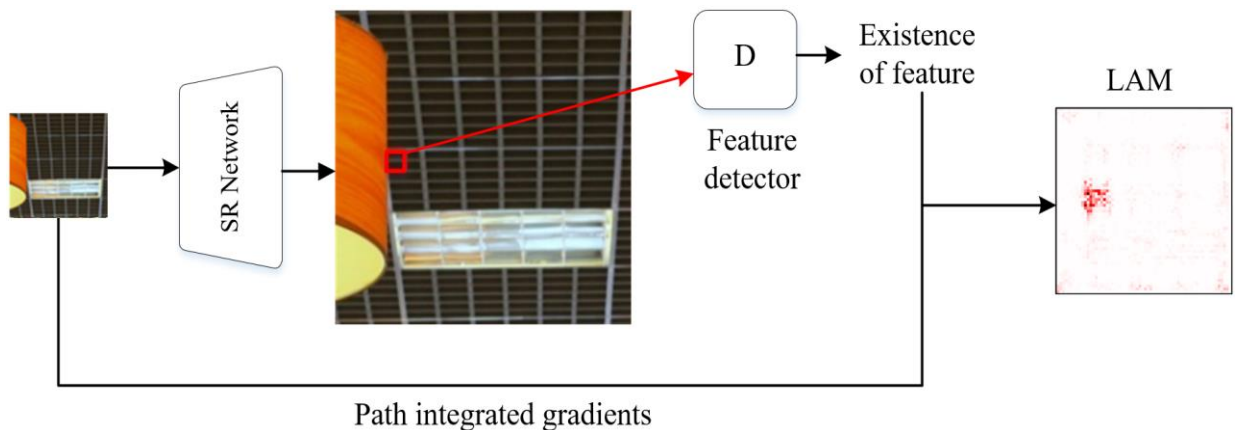


Fig. 9 Local attribution map schematic (Red pixels in LAM contribute significantly to the recovery of the boxed region).

To explore the global information modeling capability of the proposed BSGM, LAM is introduced in this paper for validation. LAM uses path integrals for gradient backpropagation to compute local features in SR concerning LR image pixels.

As shown in Fig. 9, the super-resolution reconstruction network reconstructs the LR image into the SR image. Then, a portion of the SR image is selected to extract features. Analyze which pixels of the LR image contribute most to the region's features. The denser red pixels in the LAM results indicate a large value of their contribution to recovering the features of the selected region. The LAM result in dimension $k(k = 0, 1, 2, \dots, K)$ can be calculated using the Eq. (25).

$$\text{LAM}_{F,D(\gamma)^k} := \int_0^1 \frac{\partial D(F(\gamma(\alpha)))}{\partial \gamma(\alpha)_k} \times \frac{\partial \gamma(\alpha)_k}{\partial \alpha} d\alpha, \quad (25)$$

where F 、 D denotes the super-resolution network and the local feature extractor, respectively; $\gamma(\alpha): [0,1] \rightarrow \mathbb{R}^{H \times W}$ denotes the smoothing path function, $\gamma(0)$ denotes the image obtained by blurring the input image \mathcal{I}_L' , and $\gamma(1)$ denotes the image \mathcal{I}_L of the input without blurring.

4 Experiments

This section compares the proposed network with the state-of-the-art SR networks by performing $\times 2$, $\times 3$, and $\times 4$ upscale single-image super-resolution experiments on five datasets. We quantitatively and qualitatively validate the superior performance of the proposed ESTN. Comprehensive ablation experiments are provided to evaluate the role of each component of the proposed ESTN. At last, we adopt local attribution maps to visualize and analyze the receptive fields of the proposed ESTN.

4.1 Experimental setup

4.1.1 Training details

The DIV2K SR dataset with 800 LR-HR image pairs is employed for training the proposed network. The HR image is cropped to 256×256 , and the mini-batch data size is $N = 64$. Five test datasets are employed for comparison with state-of-the-art methods: Set5 [40], Set14 [41], BSD100 [42], Urban100 [43], and Manga109 [44].

4.1.2 Training setup

In this paper, we conduct $\times 2$, $\times 3$, and $\times 4$ upscale super-resolution reconstruction tasks for training, respectively. The ESTN consists of 12 ESTM blocks with channel numbers $C = 60$. The window of BSGM is set as 4×4 , and the multi-scale window of W/SW-MSSA is set as 4×4 , 8×8 and 16×16 . In an ESTM, the attention scores calculated in W-MSSA are shared with SW-MSSA

to reduce the amount of calculation. We use bicubic downsampling to generate training image pairs and randomly crop 64 image patches of size 64×64 from the LR image as the training batch of the ESTN. We train our network with an initial learning rate of 0.0002 and attenuate the learning rate by half at the 250-th, 400-th, 425-th, 450-th, and 475-th iterations for 500 iterations. For optimization, we use the Adam optimizer based on $\beta_1 = 0.9, \beta_2 = 0.999$ and the weight decay of $1e-8$. All experiments were conducted on a server with two NVIDIA RTX3090 GPU cards.

4.1.3 Test setup

We mainly focus on the lightweight performance and reconstruction effect of the model. The lightweight performance mainly focuses on the number of parameters (Params) and float point operations (FLOPs). The FLOPs results are calculated by upscaling the SR image resolution to 1280×720 . The reconstruction effect is evaluated by the widely used PSNR[45] and SSIM[46] indicators. The SR image is converted from the RGB channel to YCbCr space. Then, the PSNR and SSIM are calculated on the Y channel.

4.2 Comparison with state-of-the-art models

This paper compares the ESTN with seven state-of-the-art single-image super-resolution lightweight SR models, including SRCNN [8], CARN [47], IMDN [48], LAPAR-A [49], ESRT [50], ELAN-light [51], and SwinIR-light [12]. The experimental data in this article are obtained by the author's weight parameters or SR results. It should be noted that since ELAN-light[51] only provides the source code, we train and obtain the results according to the code provided by the author.

4.2.1 Quantitative comparison

As shown in Table 1, the proposed ESTN achieves a state-of-the-art performance in super-resolution reconstruction for all five test sets. In the $\times 4$ upscale super-resolution results, even in the challenging-to-reconstruct Urban100 and Manga109 datasets, the ESTN yields favorable outcomes. In the $\times 4$ upscale super-resolution reconstruction results of the Manga109, the PSNR of ESTN is 0.21 dB higher than ELAN-light[51] and SwinIR-light[12]. At the same time, outstanding performance improvements have been achieved on Set5, Set14, BSD100, and Urban100 datasets. Compared with SwinIR-light[12], the ESTN contains fewer parameters and performs better than SwinIR-light.

Table 1 Quantitative comparison (average PSNR/SSIM) with lightweight image super-resolution methods on benchmark datasets.

Method	Scale	Params (K)	Set5		Set14		BSD100		Urban100		Manga109	
			PSNR	SSIM	PSNR	SSIM	PSNR	SSIM	PSNR	SSIM	PSNR	SSIM
SRCNN	×2	57	36.66	0.9542	32.42	0.9063	31.36	0.8879	29.50	0.8946	35.74	0.9661
CARN	×2	1592	37.76	0.9590	33.52	0.9166	32.09	0.8978	31.92	0.9256	38.36	0.9765
IMDN	×2	694	38.00	0.9605	33.63	0.9177	32.19	0.8996	32.17	0.9283	38.88	0.9774
LAPAR-A	×2	548	38.01	0.9605	33.62	0.9183	32.19	0.8999	32.10	0.9283	38.67	0.9772
ESRT	×2	677	38.03	0.9600	33.75	0.9184	32.25	0.9001	32.58	0.9318	39.12	0.9774
ELAN-light	×2	582	38.17	0.9611	33.94	0.9207	32.30	0.9012	32.76	0.9340	39.11	0.9782
SwinIR-light	×2	878	38.14	0.9611	33.86	0.9206	32.31	0.9012	32.76	0.9340	39.12	0.9783
ESTN (ours)	×2	863	38.23	0.9615	33.94	0.9213	32.34	0.9357	32.90	0.9357	39.27	0.9783
SRCNN	×3	57	32.75	0.9090	29.28	0.8209	28.41	0.7863	26.24	0.7989	30.59	0.9107
CARN	×3	1592	34.29	0.9255	30.29	0.8407	29.06	0.8034	28.06	0.8493	33.50	0.9440
IMDN	×3	703	34.36	0.9270	30.32	0.8417	29.09	0.8046	28.17	0.8519	33.61	0.9445
LAPAR-A	×3	544	34.36	0.9267	30.34	0.8421	29.11	0.8054	28.15	0.8523	33.51	0.9441
ESRT	×3	770	34.42	0.9268	30.43	0.8433	29.15	0.8063	28.66	0.8624	33.95	0.9455
ELAN-light	×3	590	34.61	0.9288	30.55	0.8463	29.21	0.8081	28.69	0.8624	34.00	0.9478
SwinIR-light	×3	886	34.62	0.9289	30.54	0.8463	29.20	0.8082	28.66	0.8624	33.98	0.9478
ESTN (ours)	×3	871	34.68	0.9298	30.61	0.8476	29.25	0.8096	28.82	0.8661	34.28	0.9491
SRCNN	×4	57	30.48	0.8628	27.49	0.7503	25.90	0.7101	24.52	0.7221	27.66	0.8505
CARN	×4	1592	32.13	0.8937	28.60	0.7806	27.58	0.7349	26.07	0.7837	30.47	0.9084
IMDN	×4	715	32.21	0.8948	28.58	0.7813	27.56	0.7353	26.04	0.7838	30.45	0.9075
LAPAR-A	×4	659	32.15	0.8944	28.61	0.7818	27.61	0.7366	26.14	0.7871	30.42	0.9074
ESRT	×4	751	32.19	0.8947	28.69	0.7833	27.69	0.7379	26.39	0.7962	30.75	0.9100
ELAN-light	×4	601	32.43	0.8975	28.78	0.7858	27.69	0.7406	26.47	0.7982	30.92	0.9150
SwinIR-light	×4	897	32.44	0.8975	28.77	0.7858	27.69	0.7406	26.47	0.7980	30.92	0.9150
ESTN (ours)	×4	881	32.55	0.8993	28.83	0.7876	27.71	0.7421	26.67	0.8040	31.13	0.9166

4.2.2 Qualitative comparison

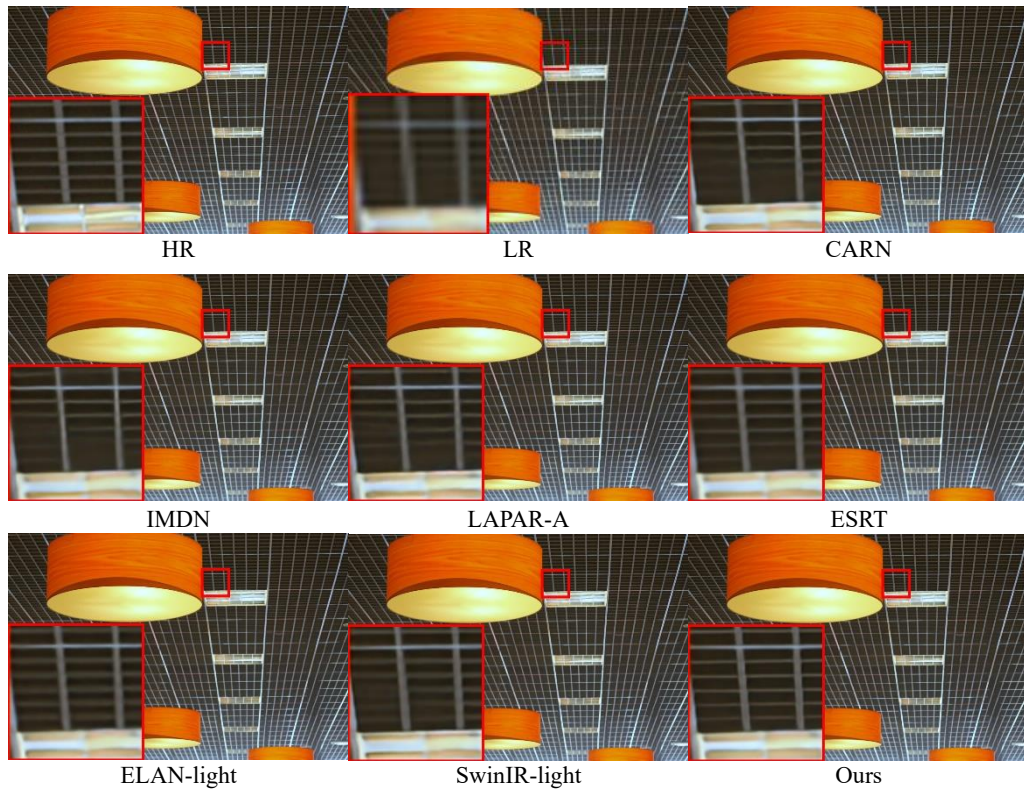


Fig. 10 Qualitative comparison of img044 with state-of-the-art lightweight SR models at x4 scale. ESTN can reconstruct clearer and sharper edge textures than other models.

As shown in Fig. 10, Fig. 11, and Fig. 12, this section qualitatively compares $\times 4$ SR results on three images (img044, img078, and img092 in Urban100). As shown in Fig. 10, the enlarged part of the SR images of CARN[47], IMDN[48], and LAPAR-A[49] based on the CNN model is very blurry, and the visual effect is poor. Although the SR images generated by the ESRT [50], ELAN-light [51], and SwinIR-light [12] models effectively recovered the texture of the images, edge blurring persisted. The ESTN is capable of restoring SR images with clear and sharp edges. As shown in Fig. 11, only the ESTN recovers the correct texture in the enlarged part of the SR image, while the SR models of CARN[47], IMDN[48], LAPAR-A[49], ESRT[50], ELAN-light[51], and SwinIR-light[12] all recover wrong textures in the SR image amplification part. In Fig. 12, only the ESTN can consider image texture recovery in several directions in the SR image enlarged part. The texture directions of SR images recovered by CARN[47], IMDN[48], and LAPAR-A[49] based on CNN are completely wrong and blurred. The ESRT[50], ELAN-light[51], and SwinIR-light[12] are unable to take care of texture recovery in different directions simultaneously.

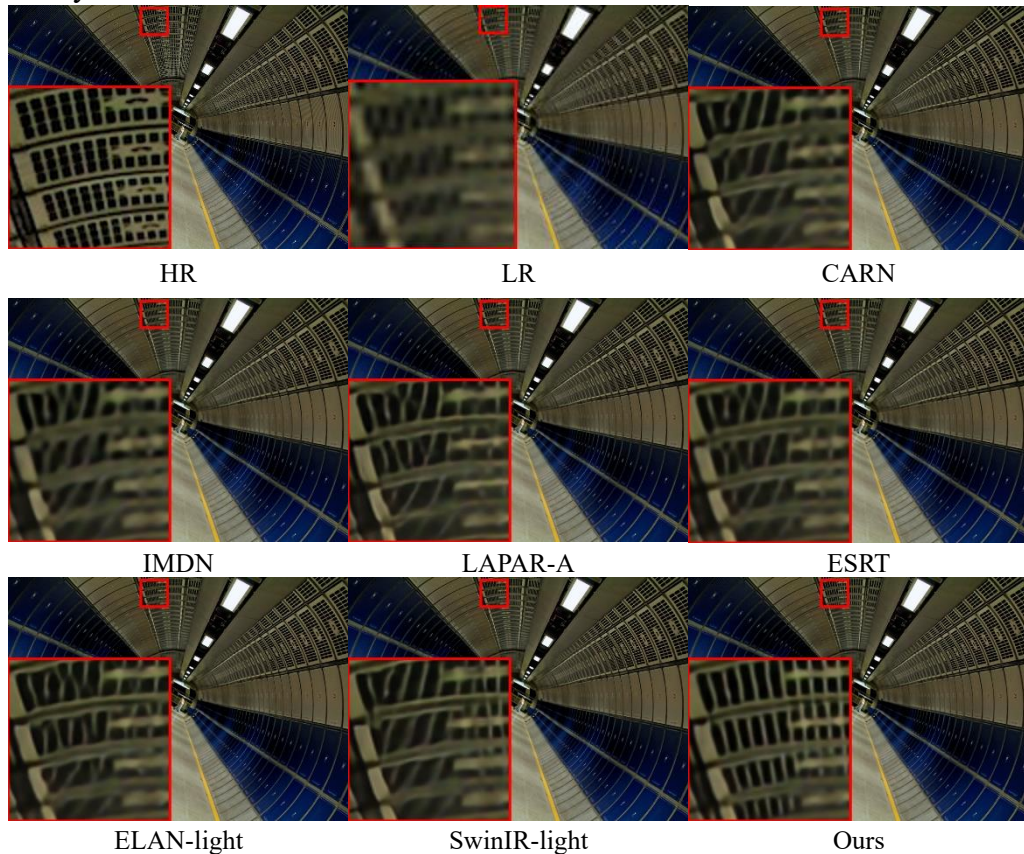


Fig. 11 Qualitative comparison of img078 with state-of-the-art lightweight SR models at $\times 4$ scale. ESTN can reconstruct more accurate texture information than other models.

The CNN-based SR models may have bad reconstruction effects due to the small receptive field of CNN. Compared with the CNN-based SR model, the Transformer-based and Swin Transformer-based models have certain improvements in performance. However, there is still

room for improvement. The proposed model starts by improving the receptive field of the model. It introduces sparse global perception, so the model has a global receptive field. In this way, the restored SR image has a more accurate texture than traditional Swin Transformer-based SR models.

The above qualitative and quantitative analysis shows that the model proposed is better than other advanced methods. The reconstructed SR image via the ESTN is closer to the HR image than the ones obtained by other networks.

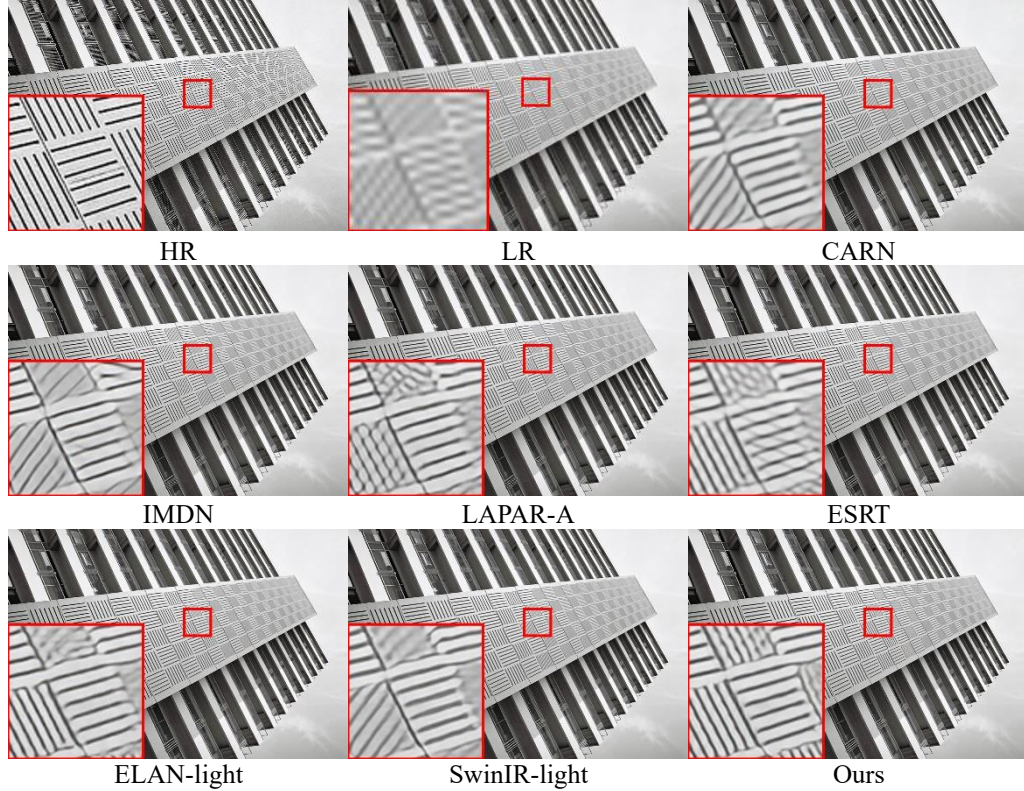


Fig. 12 Qualitative comparison of img092 with state-of-the-art lightweight SR models at x4 scale. The proposed ESTN network can reconstruct more comprehensive and accurate edge information than other models.

4.3 Ablation studies

To better understand how ESTN, we conducted comprehensive ablation experiments to evaluate the role of each component of ESTN, as well as experimental results of different designs of low-parameter channel attention modules. The models in the ablation experiments were all trained with a batch size of 4, and the remaining parameters are consistent with the experimental setup section.

4.3.1 ESTN ablation study

The number of float point operations FLOPs and the number of parameters Params are reference indicators for measuring lightweight networks. Therefore, to visually demonstrate the efficiency of the proposed improved strategy, we conduct ablation experiments with and without BSGM and the LRCAB. As shown in Table 2, the PSNR of the network with the BSGM module

is improved by 0.12 dB compared with the ELAN-light[51] network, the number of parameters only increases by 114 K, and the total number of float point operations increases by 17 G. Compared with the ELAN-light[51] network with BSGM, the PSNR of the network with LRCAB module is improved by 0.09 dB, the total number of float point operations only increases by 4 G, and the number of parameters increases by 168 K.

Table 2 Module ablation experiment of dataset manga109 at x4 resolution.

Method	ELAN-light	+BSGM	+BSGM +LRCAB
FLOPs	54G	71G	75G
Params	601k	715k	883k
PSNR (dB)	30.67	30.78	30.87
SSIM	0.9112	0.9120	0.9128

4.3.2 Low-parametric residual channel attention ablation study

Table 3 Channel attention module ablation experiment of dataset manga109 at x4 resolution.

Design	Original RCAB	Two Conv1×1 RCAB	Two Conv3×3 RCAB	Conv1×1&Conv3×3 RCAB(LRCAB)
FLOPs	71G	79G	72G	75G
Params	863K	729K	1036K	883K
PSNR	30.78	30.83	30.88	30.87
SSIM	0.9119	0.9119	0.9130	0.9128

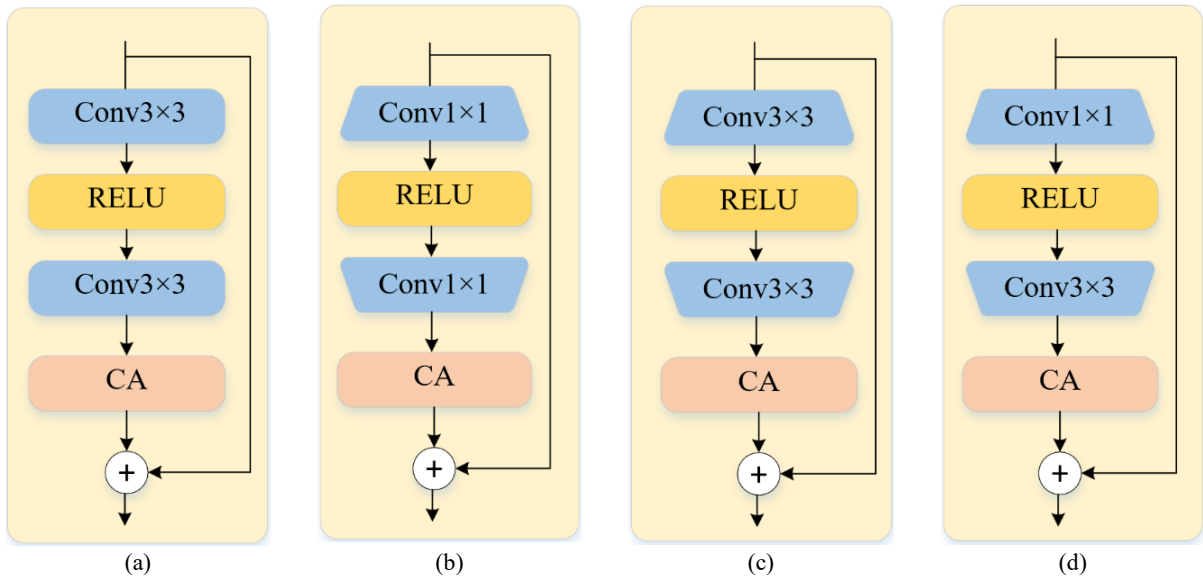







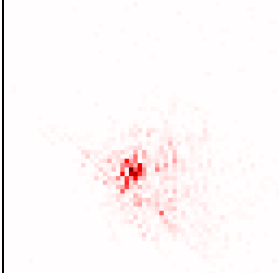

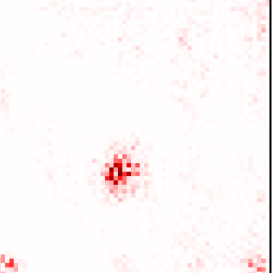
Fig. 13 Comparison of low-parameter residual channel attention modules with other channel attention modules: (a) Original RCAB; (b) Two Conv1×1 RCAB; (c) Two Conv3×3 RCAB; (d) Conv1×1&Conv3×3 RCAB(LRCAB).

As Fig. 13 (a)-(d) shows the efficiency of LRCAB, we give four channel attentions for comparison. As shown in Table 3, the three redesigned channel attention blocks in Fig. 13 (b)-(d)

effectively improve the PSNR metrics compared to the Residual Channel Attention Block (RCAB). The module in Fig. 13 (b) employs two 1×1 convolutional transformations of the feature dimensions before computing the channel attention, with no improvement in performance metrics but a decrease in the number of parameters. The module in Fig. 13 (c) adopts two 3×3 convolutional transform feature dimensions before calculating the channel attention, which improves the performance metrics but increases the number of parameters by 173 K compared to the original RCAB. The LRCAB in Fig. 13 (d) uses 1×1 convolution and 3×3 convolution to transform the feature dimensions before computing the channel attention. This approach improves the performance metrics while increasing the number of parameters and the number of float-point operations over the original RCAB by only 20 K and 4 G, respectively.

4.4 Analysis of attribution results

As shown in Fig. 14, we show SR and LAM results based on the Transformer model. The red pixels in the LAM results indicate that they have a greater impact on the recovery results of the selected area of interest. Based on the Swin Transformer, the LAM results of ELAN-light[51] and SwinIR-light [12] show that red pixels are mainly distributed around the selected area, and the global perception capability is relatively limited. As can be seen from the LAM results of the ESTN model, except for the dense red pixels around the selected area of interest, the entire area is sparsely distributed with red pixels. This shows that our proposed model can use the information of the entire input LR image to restore the selected area of interest, which is beneficial for reconstructing accurate and sharp textures.

			ELAN-light	SwinIR-light	Ours
HR Image		SR results			
LR Image		LAM results			

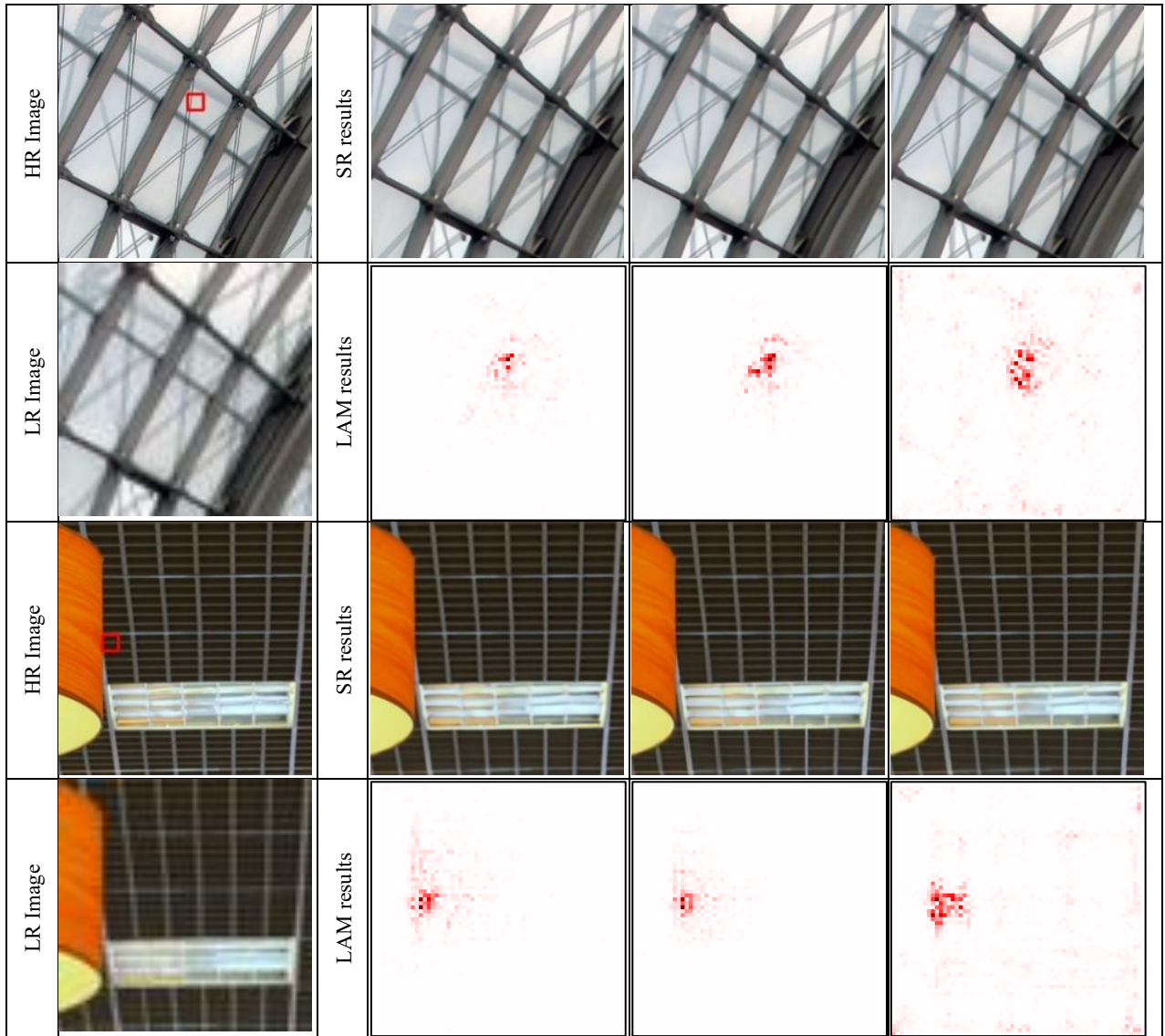


Fig. 14 SR results and local attribution map results for the Swin Transformer-based lightweight SR network (The local attribution map results visualize the influence of different pixels in the SR results.)

5 Conclusion

An image super-resolution network with alternating aggregation of local-global features is proposed in this paper. On the one hand, the shift convolution is introduced to realize local feature aggregation and the interaction between local spatial and channel information. On the other hand, the BSGM, W-MSSA, SW-MSSA, and LRCAB are brought in to enable global feature aggregation and the interaction between global spatial and channel information. The experimental results show that ESTN achieves notable performance improvements on the Set5, Set14, BSD100, Urban100, and Manga109 image super-resolution datasets. The proposed network introduces several novel aspects, including:

(1) Local-global feature alternation aggregation achieves comprehensive spatial and channel interaction, effectively enhancing the non-linear mapping performance of the network.

(2) The multi-scale window attention mechanism is employed to construct a more flexible spatial long-range feature dependency. In this way, we mitigate the challenges associated with the high computational complexity of global window operations and the limited receptive field size of fixed windows.

(3) The LRCAB is proposed to address the issue of inter-channel redundancy in traditional feed-forward networks. This module allocates channel attention to each channel without significantly increasing the network parameters.

(4) LAM is introduced to visualize attribution results for selected regions. The experiments reveal the reasons behind the excellent image reconstruction performance of the proposed ESTN. The larger receptive field enables the model to effectively leverage information from LR images for image super-resolution reconstruction.

It should be noted that there is room for optimization in terms of computational complexity for the proposed algorithm. Given the network's relatively lengthy forward computation time, the next step could involve optimizing BSGM to reduce the overall runtime.

References

1. J. Wang, Z. Shao, X. Huang, et al. A deep unfolding method for satellite super resolution[J]. *IEEE Transactions on Computational Imaging*, 2022, 8: 933-944.
2. Z. Gao and J. Chen. Maritime infrared image super-resolution using cascaded residual network and novel evaluation Metric[J]. *IEEE Access*, 2022, 10: 17760-17767.
3. Q. Liu, R. Jia, Y. Liu, et al. Infrared image super-resolution reconstruction by using generative adversarial network with an attention mechanism[J]. *Applied Intelligence*, 2021, 51: 2018-2030.
4. Y. Zhang, K. Li, K. Li, et al. MR image super-resolution with squeeze and excitation reasoning attention network[C]. *Proceedings of the IEEE/CVF Conference on Computer Vision and Pattern Recognition*, Nashville, TN, USA, 2021, 13425-13434.
5. D. Khaledyan, A. Amirany, K. Jafari, et al. Low-cost implementation of bilinear and bicubic image interpolation for real-time image super-resolution[C]. *2020 IEEE Global Humanitarian Technology Conference (GHTC)*, 2020, 1-5.
6. J. Huang, L. Wang, J. Qin, et al. Super-resolution of intravoxel incoherent motion imaging based on multisimilarity[J]. *IEEE Sensors Journal*, 2020, 20(18): 10963-10973.
7. J. Jin, L. Dong, Y. Jiang, et al. Image super resolution based on gradient constrained POCS method[C]. *Journal of Physics: Conference Series*, 2019, 032033.
8. C. Dong, C. C. Loy, K. He, et al. Learning a deep convolutional network for image super-resolution[C]. *Computer Vision - ECCV 2014*, Zurich, Switzerland, 2014, 184-199.
9. K. Simonyan and A. Zisserman. Very deep convolutional networks for large-scale image recognition[C]. *International Conference on Learning Representations*, San Diego, CA, USA, 2015, 1-14.
10. K. He, X. Zhang, S. Ren, et al. Deep residual learning for image recognition[C]. *Proceedings of the IEEE Conference on Computer Vision and Pattern Recognition*, Las Vegas,

- NV, USA, 2016, 770–778.
11. C. Ledig, L. Theis, F. Huszár, et al. Photo-realistic single image super-resolution using a generative adversarial network[C]. Proceedings of the IEEE Conference on Computer Vision and Pattern Recognition, Honolulu, HI, USA, 2017, 4681–4690.
 12. J. Liang, J. Cao, G. Sun, et al. Swinir: Image restoration using swin transformer[C]. Proceedings of the IEEE/CVF International Conference on Computer Vision, Montreal, QC, Canada, 2021, 1833–1844.
 13. J. Fang, H. Lin, X. Chen, et al. A hybrid network of cnn and transformer for lightweight image super-resolution[C]. Proceedings of the IEEE/CVF Conference on Computer Vision and Pattern Recognition, New Orleans, LA, USA, 2022, 1103–1112.
 14. H. Choi, J. Lee, and J. Yang. N-gram in swin transformers for efficient lightweight image super-resolution[C]. Proceedings of the IEEE/CVF Conference on Computer Vision and Pattern Recognition, Vancouver Convention Center, Sun Jun 18th through Thu the 22nd, 2023, 2071–2081.
 15. I. O. Tolstikhin, N. Houlsby, A. Kolesnikov, et al. Mlp-mixer: An all-mlp architecture for vision[J]. Advances in neural information processing systems, 2021, 34: 24261–24272.
 16. A. Vaswani, N. Shazeer, N. Parmar, et al. Attention is all you need[C]. Advances in Neural Information Processing Systems, Long Beach, California, USA, 2017, 6000 – 6010.
 17. Z. Chen, Y. Zhang, J. Gu, et al. Dual Aggregation Transformer for Image Super-Resolution[C]. Proceedings of the IEEE/CVF International Conference on Computer Vision, Paris, France, Sep 30—Oct 6, 2023, 12312–12321.
 18. X. Chen, X. Wang, J. Zhou, et al. Activating more pixels in image super-resolution transformer[C]. Proceedings of the IEEE/CVF Conference on Computer Vision and Pattern Recognition, Vancouver Convention Center, Sun Jun 18th through Thu the 22nd, 2023, 22367–22377.
 19. N. Carion, F. Massa, G. Synnaeve, et al. End-to-end object detection with transformers[C]. Computer Vision – ECCV 2020: 16th European Conference, Glasgow, UK, August 23 – 28, Proceedings, Part I 16, 2020, 213–229.
 20. A. Dosovitskiy, L. Beyer, A. Kolesnikov, et al. An image is worth 16x16 words: Transformers for image recognition at scale[C]. International Conference on Learning Representations, Austria Vienna, 2021, 1–21.
 21. A. Arnab, M. Dehghani, G. Heigold, et al. Vivit: A video vision transformer[C]. Proceedings of the IEEE/CVF International Conference on Computer Vision, Montreal, QC, Canada, 2021, 6836–6846.
 22. S. Li, G. Wang, H. Zhang, et al. SDRSwin: A residual swin transformer network with saliency detection for infrared and visible image fusion[J]. Remote Sensing, 2023, 15(18): 4467.
 23. H. Chen, Y. Wang, T. Guo, et al. Pre-trained image processing transformer[C]. Proceedings of the IEEE/CVF Conference on Computer Vision and Pattern Recognition, Nashville, TN, USA, 2021, 12299–12310.
 24. Z. Wang, X. Cun, J. Bao, et al. Uformer: A general u-shaped transformer for image restoration[C]. Proceedings of the IEEE/CVF Conference on Computer Vision and Pattern Recognition, New Orleans, LA, USA, 2022, 17683–17693.
 25. E. Xie, W. Wang, Z. Yu, et al. SegFormer: Simple and efficient design for semantic segmentation with transformers[J]. Advances in Neural Information Processing Systems,

- 2021, 34: 12077–12090.
26. R. Xu, H. Xiang, Z. Tu, et al. V2X-ViT: Vehicle-to-everything cooperative perception with vision transformer[C]. Computer Vision - ECCV 2022: 17th European Conference, Tel Aviv, Israel, October 23 - 27, 2022, Proceedings, Part XXXIX, 2022, 107–124.
 27. Z. Liu, Y. Lin, Y. Cao, et al. Swin transformer: Hierarchical vision transformer using shifted windows[C]. Proceedings of the IEEE/CVF International Conference on Computer Vision, Montreal, QC, Canada, 2021, 10012–10022.
 28. H. Liu, Z. Dai, D. So, et al. Pay attention to mlps[J]. Advances in Neural Information Processing Systems, 2021, 34: 9204–9215.
 29. Z. Tu, H. Talebi, H. Zhang, et al. Maxim: Multi-axis mlp for image processing[C]. Proceedings of the IEEE/CVF Conference on Computer Vision and Pattern Recognition, New Orleans, LA, USA, 2022, 5769–5780.
 30. J. Gu and C. Dong. Interpreting super-resolution networks with local attribution maps[C]. Proceedings of the IEEE/CVF Conference on Computer Vision and Pattern Recognition, Nashville, TN, USA, 2021, 9199–9208.
 31. X. Wang, K. Yu, S. Wu, et al. Esrgan: Enhanced super-resolution generative adversarial networks[C]. Proceedings of the European Conference on Computer Vision (ECCV), Munich, Germany, 2018, 63–79.
 32. Y. Zhang, K. Li, K. Li, et al. Image super-resolution using very deep residual channel attention networks[C]. Proceedings of the European Conference on Computer Vision (ECCV), Munich, Germany, 2018, 286–301.
 33. J. Li, Q. Lv, W. Zhang, et al. Multi-attention multi-image super-resolution transformer (MAST) for remote sensing[J]. Remote Sensing, 2023, 15(17): 4183.
 34. D. Hendrycks and K. Gimpel. Gaussian error linear units (gelus)[J]. arXiv preprint arXiv:1606.08415, 2016.
 35. J. L. Ba, J. R. Kiros, and G. E. Hinton. Layer normalization[J]. arXiv preprint arXiv:1607.06450, 2016.
 36. B. Wu, A. Wan, X. Yue, et al. Shift: A zero flop, zero parameter alternative to spatial convolutions[C]. Proceedings of the IEEE Conference on Computer Vision and Pattern Recognition, Salt Lake City, UT, USA, 2018, 9127–9135.
 37. W. Shi, J. Caballero, F. Huszár, et al. Real-time single image and video super-resolution using an efficient sub-pixel convolutional neural network[C]. Proceedings of the IEEE Conference on Computer Vision and Pattern Recognition, Las Vegas, NV, USA, 2016, 1874–1883.
 38. D. P. Kingma and J. Ba. Adam: A method for stochastic optimization[J]. arXiv preprint arXiv:1412.6980, 2014.
 39. V. Nair and G. E. Hinton. Rectified linear units improve restricted boltzmann machines[C]. Proceedings of the 27th international conference on machine learning (ICML-10), 2010, 807–814.
 40. M. Bevilacqua, A. Roumy, C. Guillemot, et al. Low-complexity single image super-resolution based on nonnegative neighbor embedding[C]. British Machine Vision Conference, 2012, 1–10.
 41. R. Zeyde, M. Elad, and M. Protter. On single image scale-up using sparse-representations[C]. Curves and Surfaces: 7th International Conference, Avignon, France, June 24–30, 2010, Revised Selected Papers 7, 2012, 711–730.

42. D. Martin, C. Fowlkes, D. Tal, et al. A database of human segmented natural images and its application to evaluating segmentation algorithms and measuring ecological statistics[C]. Proceedings Eighth IEEE International Conference on Computer Vision. ICCV 2001, 2001, 416-423.
43. J.-B. Huang, A. Singh, and N. Ahuja. Single image super-resolution from transformed self-exemplars[C]. Proceedings of the IEEE Conference on Computer Vision and Pattern Recognition, 2015, 5197-5206.
44. Y. Matsui, K. Ito, Y. Aramaki, et al. Sketch-based manga retrieval using mangal09 dataset[J]. Multimedia Tools and Applications, 2017, 76: 21811-21838.
45. A. Ichigaya, M. Kurozumi, N. Hara, et al. A method of estimating coding PSNR using quantized DCT coefficients[J]. IEEE Transactions on circuits and systems for video technology, 2006, 16(2): 251-259.
46. Z. Wang, A. C. Bovik, H. R. Sheikh, et al. Image quality assessment: from error visibility to structural similarity[J]. IEEE transactions on image processing, 2004, 13(4): 600-612.
47. N. Ahn, B. Kang, and K.-A. Sohn. Fast, accurate, and lightweight super-resolution with cascading residual network[C]. Proceedings of the European Conference on Computer Vision (ECCV), Munich, Germany, 2018, 252-268.
48. Z. Hui, X. Gao, Y. Yang, et al. Lightweight image super-resolution with information multi-distillation network[C]. Proceedings of the 27th Acm International Conference on Multimedia, 2019, 2024-2032.
49. W. Li, K. Zhou, L. Qi, et al. Lpar: Linearly-assembled pixel-adaptive regression network for single image super-resolution and beyond[J]. Advances in Neural Information Processing Systems, 2020, 33: 20343-20355.
50. Z. Lu, J. Li, H. Liu, et al. Transformer for single image super-resolution[C]. 2022 IEEE/CVF Conference on Computer Vision and Pattern Recognition Workshops (CVPRW), 2022, 456-465.
51. X. Zhang, H. Zeng, S. Guo, et al. Efficient long-range attention network for image super-resolution[C]. European Conference on Computer Vision, Tel-Aviv, Israel, Berlin: Springer, 2022, 649-667.